

Nanomechanical probing and strain tuning of the Curie temperature in suspended $\text{Cr}_2\text{Ge}_2\text{Te}_6$ heterostructures

Makars Šiškins,¹ Samer Kurdi,¹ Martin Lee,¹ Benjamin J. M. Slotboom,¹ Wenyu Xing,² Samuel Mañas-Valero,³ Eugenio Coronado,³ Shuang Jia,² Wei Han,² Toeno van der Sar,¹ Herre S. J. van der Zant,¹ and Peter G. Steeneken^{1,4,*}

¹*Kavli Institute of Nanoscience, Delft University of Technology, Lorentzweg 1, 2628 CJ, Delft, The Netherlands*

²*International Center for Quantum Materials, Peking University, 5 Summer Palace Road, 100871 Beijing, China*

³*Instituto de Ciencia Molecular (ICMol), Universitat de València, c/Catedrático José Beltrán 2, 46980 Paterna, Spain*

⁴*Department of Precision and Microsystems Engineering, Delft University of Technology, Mekelweg 2, 2628 CD, Delft, The Netherlands*

Two-dimensional (2D) magnetic materials with strong magnetostriction are interesting systems for strain-tuning the magnetization, enabling potential for realizing spintronic and nanomagnetic devices. Realizing this potential requires understanding of the magneto-mechanical coupling in the 2D limit. In this work, we suspend thin $\text{Cr}_2\text{Ge}_2\text{Te}_6$ layers, creating nanomechanical membrane resonators. We probe its mechanical and magnetic properties as a function of temperature and strain. Pronounced signatures of magneto-elastic coupling are observed in the temperature-dependent resonance frequency of these membranes near T_C . We further utilize $\text{Cr}_2\text{Ge}_2\text{Te}_6$ in heterostructures with thin layers of WSe_2 and FePS_3 , which have positive thermal expansion coefficients, to compensate the negative thermal expansion coefficient of $\text{Cr}_2\text{Ge}_2\text{Te}_6$ and quantitatively probe the corresponding T_C . Finally, we induce a strain of 0.016% in a suspended heterostructure via electrostatic force and demonstrate a resulting enhancement of T_C by 2.5 ± 0.6 K in the absence of an external magnetic field.

The recent discovery of long range order in two-dimensional (2D) (anti)ferromagnets [1–3] has triggered extensive studies of 2D materials to experimentally probe magnetism of reduced dimensionality [4]. One material of particular interest is $\text{Cr}_2\text{Ge}_2\text{Te}_6$ (CGT) – a semiconducting ferromagnet with a bulk Curie temperature, T_C , $\sim 60 - 66$ K [2, 5] with inter- and intra-layer ferromagnetic coupling for any number of layers [2]. Recent progress has been made in manipulating the magnetic order of CGT using electrostatic gating [6, 7], magnetic field [2, 8], pressure [9, 10], ion intercalation [11], and via spin-orbit torque [12, 13]. Mechanical strain offers another degree of freedom for such manipulation as bulk CGT was recently shown to exhibit strong spin-lattice coupling [9, 14] and a negative thermal expansion coefficient near T_C [5], which is common amongst bulk chromium-based magnetic van der Waals crystals, like CrI_3 , CrCl_3 , CrBr_3 and $\text{Cr}_2\text{Si}_2\text{Te}_6$ [15–18]. However, the coupling between magnetic order and strain in thin CGT has not been studied experimentally, as strain is a difficult parameter to control in substrate-supported ultrathin layers [19, 20].

Emerging nanomechanical methods allow for high-precision strain manipulation and control when 2D materials are suspended forming ultrathin membrane resonators [21, 22]. Due to the combination of low mass with high strength, these membranes find potential use

in high-performance devices [21, 23] and in a wide range of sensor applications [24]. The resonance frequency of these membranes can be tuned over a large range by strain [21], which can be controlled both statically [25] and dynamically [21, 22]. Moreover, the difference between the thermal expansion coefficient of suspended 2D material layers and the substrate [26, 27] or other materials in a heterostructure [28, 29] provides additional routes for strain engineering, leading to either stretching or compressing ultrathin layers. Nanomechanical strain can also be used to probe magnetic states of membrane material [26] and switch between these states [29, 30]. It is the relation between strain, a material’s thermal expansion coefficient and its magnetic properties which results in the coupling between mechanical and magnetic degrees of freedom, that allows investigation of magnetic phase transitions in 2D layered material membranes [26, 29].

Here, we demonstrate that the magnetic phase transition of suspended thin CGT membranes can be probed mechanically via the temperature-dependent resonance frequency. CGT is known to exhibit high magnetostriction, i.e. a strong magneto-elastic coupling between magnetic order and the lattice [5, 9, 14], that deforms the crystal near T_C [5]. Thus, to control the strain in thin CGT flakes and deterministically probe the transition temperature, we choose other 2D material layers, WSe_2 and FePS_3 , with positive thermal expansion coefficient and integrate them to form heterostructure membranes with CGT [28, 31–33], which are important to compensate CGT’s negative thermal expansion [5]. We then use these heterostructure membranes to probe and analyze

* e-mail: m.siskins-1@tudelft.nl; t.vandersar@tudelft.nl;
h.s.j.vanderzant@tudelft.nl; p.g.steeneken@tudelft.nl

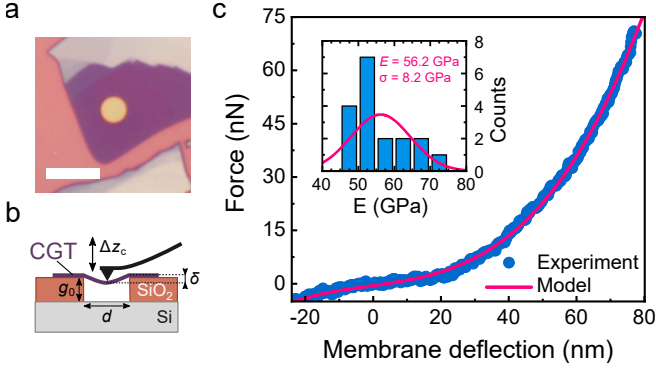


FIG. 1. Force indentation of suspended membranes of CGT. **a** An optical image of a $9.5 \pm 0.3 \text{ nm}$ thin CGT membrane with a radius $r = 2 \mu\text{m}$. Scale bar: $8 \mu\text{m}$. **b** A schematic of the membrane deflection by a cantilever tip. Δz_c is the cantilever deflection, $g_0 = 285 \text{ nm}$ the separation between the membrane and the bottom Si substrate, d the membrane diameter, and δ the membrane deflection. **c** A force versus membrane deflection plot. Experimental data (filled blue circles) are fit by the point-force deflection of a circular membrane model of equation (1) (solid magenta line). The inset shows a histogram of the Young's moduli extracted from 18 CGT membranes of $9.5 - 30.1 \text{ nm}$ thicknesses, which were used to obtain the mean value of the Young's modulus E and corresponding standard deviation σ .

the effect of the mutual interaction between the different 2D materials and CGT, and study the effect of electrostatically induced strain on the ferromagnetic order near T_C .

RESULTS

Mechanical properties of CGT membranes.

The force-deflection curve of suspended membranes contains information about mechanical properties of the material. Thus, we first study thin layers of CGT by a static deflection method [25, 34]. We fabricate a free-standing membrane by suspending a mechanically exfoliated thin CGT flake over a circular hole (Fig. 1a). We then apply the atomic force microscopy (AFM) force nanoindentation method [25, 34] to indent the centre of the membrane with the tip of an AFM cantilever to cause a deflection of the membrane δ , as shown in Fig. 1b. The force applied to the centre of the membrane, F , is proportional to the stiffness k_c of the cantilever used and its deflection, Δz_c . Using cantilevers with calibrated stiffnesses, we record the force versus membrane deflection curves of this membrane, as depicted in Fig. 1c with filled blue circles. The observed trend can be described by the point-force deflection model for a circular membrane, assuming negligible tip radius compared to the membrane

diameter [25, 34]:

$$F = \left(\frac{4\pi E}{3(1-\nu^2)} \frac{h^3}{r^2} \right) \delta + (n_0\pi) \delta + \left(\frac{q^3 E h}{r^2} \right) \delta^3, \quad (1)$$

where E is the Young's modulus of the membrane, r the membrane radius, h the membrane thickness, $\nu = 0.22$ the Poisson ratio of CGT [35], n_0 the pre-tension and $q = 1/(1.05 - 0.15\nu - 0.16\nu^2)$ is a dimensionless geometrical parameter. To our knowledge, the Young's modulus of CGT has not been experimentally studied. We therefore extract its Young's modulus E_{CGT} from the experimental data using equation (1), as shown in Fig. 1c by the solid magenta line. To obtain a more reliable estimate of E_{CGT} , we measure 18 different membranes of varying thicknesses ($h = 9.5 - 30.1 \text{ nm}$) and radii ($r = 1 - 2.5 \mu\text{m}$). We find a mean value, $E_{\text{CGT}} = 56.2 \pm 8.2 \text{ GPa}$, as shown in the inset of Fig. 1c. The obtained value of E_{CGT} is consistent with the calculated [36] 2D Young's modulus of CGT, $E_{2\text{D}} = 41.8 \text{ Nm}^{-1}$, which yields to $E = E_{2\text{D}}/h_{2\text{D}} = 61.0 \text{ GPa}$, in which $h_{2\text{D}}$ is the single-layer thickness, taken as a third of that of the unit cell of CGT [5]: $h_{2\text{D}} = 2.056 \text{ nm}/3 \approx 0.685 \text{ nm}$. The standard deviation for our measurements is comparable to that reported in similar experiments on other 2D material membranes [25, 34]. We also found no layer number dependence for the studied range of thicknesses [37].

Resonating membranes.

In order to study the coupling between the magnetic phase and the mechanical motion, we further investigate the dynamic nanomechanical properties of these membranes as a function of temperature. The temperature dependence of the mechanical resonances of the magnetic membranes is sensitive to changes in the magnetisation of the 2D layers [29] and the magnetic phase, via a mechanism that couples the specific heat to the membrane tension via the thermal expansion coefficient [26]. Thus, by observing changes in motion of the membrane at T_C it is possible to probe the ferromagnetic to paramagnetic transition via the mechanical resonance frequency [26]. To do this, we use a laser interferometry technique [26, 38] (Fig. 2a and Experimental Section). A CGT membrane (see the inset of Fig. 2b) is placed in the chamber of an optical cryostation. We use a power-modulated blue laser to opto-thermally excite a fundamental resonance mode of the membrane, and a red laser to measure the change in the reflected signal due to the subsequent displacement of the membrane.

We first measure the resonance peak of the fundamental membrane mode at $T = 4 \text{ K}$ (blue circles in Fig. 2b). We fit the experimental data to a harmonic oscillator model (solid magenta line in Fig. 2b) to determine the frequency of the fundamental membrane mode, f_0 . Subsequently, while recording $f_0(T)$ we heat the sample to $T = 78 \text{ K}$, above the expected T_C of 66 K [2, 5], and cool it down to $T = 4 \text{ K}$. We plot the experimental data

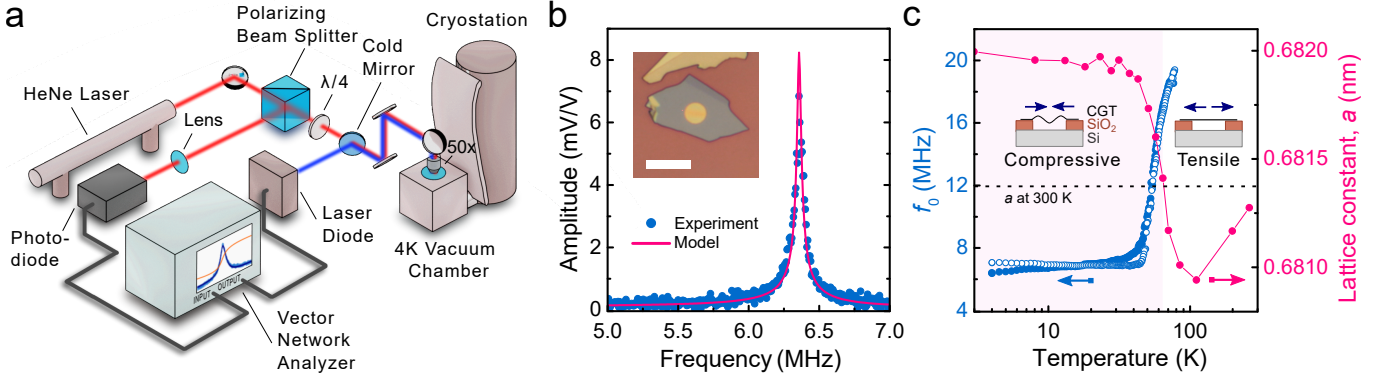


FIG. 2. CGT membrane characterization using laser interferometry. **a** Schematic diagram of the laser interferometry setup. **b** Filled blue circles - measured amplitude of the fundamental resonance peak at $T = 4$ K. Solid magenta line - fit to a linear harmonic oscillator model. The inset shows an optical image of a 17.4 ± 0.3 nm thin CGT membrane of $2 \mu\text{m}$ radius. Scale bar: $8 \mu\text{m}$. **c** The comparison of the measured resonance frequency f_0 of the thin film shown in (b) and the lattice constant of bulk CGT as a function of temperature. The filled and open blue circles represent the measured data during heating and cooling cycles respectively. The connected magenta circles represent the lattice constant a of bulk CGT as measured by Carteaux et al [5]. The dashed black horizontal line represents a at $T = 300$ K. The insets show schematics of membrane stretching or buckling at tensile or compressive strain, on the left and right respectively. The pink region indicates the temperature range where compressive strain is dominant and is a guide to an eye.

for the heating (filled blue circles) and the cooling (open blue circles) cycle in Fig. 2c. As the CGT membrane is cooled through the T_C , its resonance frequency f_0 reduces from 19.3 MHz at 78 K to 6.3 MHz at 4 K. To describe the $f_0(T)$ behaviour of CGT, we model the resonance frequency of a circular membrane as:

$$f_0(T) = \sqrt{\left(\frac{2.4048}{2\pi r}\right)^2 \frac{n_{\text{th}}(T)}{\rho h} + f_0^2(T_0)}, \quad (2)$$

where $f_0(T_0)$ is the resonance frequency at a reference temperature T_0 (e.g. room temperature) due to the contribution of the pre-tension and the bending rigidity, ρ the mass density, $n_{\text{th}}(T) = \frac{Eh}{(1-\nu)}\epsilon_{\text{th}}$ the thermally accumulated tension, $\epsilon_{\text{th}} = -\int_{T_0}^{T_i} (\alpha_{\text{CGT}}(T) - \alpha_{\text{Si}}(T)) dT$ the thermal strain at an arbitrary temperature T_i [26, 27], $\alpha_{\text{Si}}(T)$ the literature values for thermal expansion coefficient of Si substrate [39], and $\alpha_{\text{CGT}}(T)$ the temperature dependent thermal expansion coefficient of CGT. Thus, we attribute the observed $f_0(T)$ trend to a large change in the in-plane lattice constants of the unit cell and the resulting negative $\alpha_{\text{CGT}}(T)$ near the phase transition, which was also previously reported for bulk CGT [5]. This anomalous lattice expansion, when cooling down from the paramagnetic to the ferromagnetic state, is related to the strong magnetostriction effect at the ferromagnetic ordering temperature T_C in CGT [5, 14] that causes a substantial drop in strain $\epsilon_{\text{th}}(T)$ and a corresponding reduction of the membrane tension near T_C .

In Fig. 2c we also plot the change of the in-plane lattice constant, a , of bulk CGT, experimentally obtained by Carteaux et al. [5], as a function of temperature and compare it with the observed resonance frequency. The

lattice constant a is shown to be smaller at room temperature (indicated by the black horizontal dashed line) in comparison to temperatures below the paramagnetic to ferromagnetic phase transition (~ 66 K). Since the lattice constant increases, the suspended part of the flake effectively has a larger volume at $T < T_C$ than at room temperature, indicating a switch from tensile to compressive strain, as indicated by the pink region in Fig. 2c. In this temperature range, the compressively strained suspended flake is likely to sag, irreproducibly wrinkle or buckle, which possibly explains a different warming and cooling trend for the resonance frequency $f_0(T)$. Buckling of magnetic layers itself is interesting for the development of reprogrammable mechanical memory devices at nano- and micro-scale [40] utilizing the bi-stable states of a buckled flake [41, 42]. However, due to the changing resonance mode shape in the compressive strain regime, and the potential wrinkling, equation (2) is not reliable for $T < T_C$. Thus, a comprehensive analysis of $f_0(T)$ near and below the phase transition [26] cannot be applied to resonators made of bare CGT.

Tensile strain in heterostructure membranes.

To prevent the compressive strain that can lead to wrinkling in CGT membranes, and controllably probe $f_0(T)$ near and below its phase transition temperature, we fabricate a suspended membrane heterostructure composed of CGT and WSe_2 flakes, shown in Fig. 3. WSe_2 is a material with well-known mechanical properties [27, 43, 44] that does not undergo a phase transition from 4 to 300 K [44]. In the heterostructure, its positive thermal expansion coefficient $\alpha_{\text{WSe}_2}(T)$ counteracts

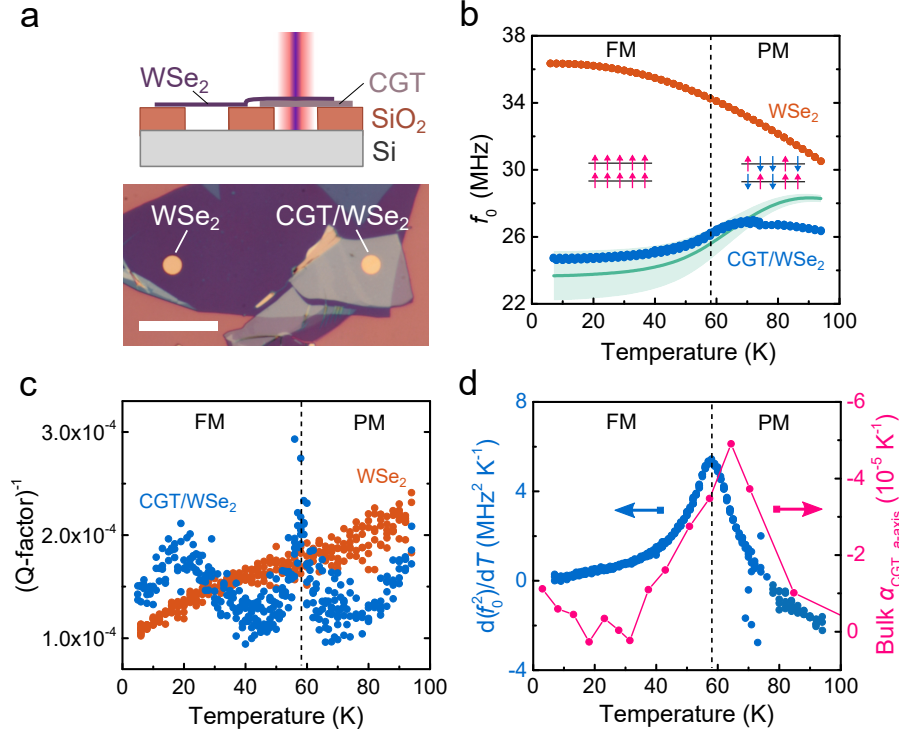


FIG. 3. Mechanical properties of a suspended CGT/WSe₂ (16.7 ± 0.3 nm/ 6.9 ± 0.1 nm) heterostructure membrane with a radius $r = 2$ μm. **a** Top panel: Schematic cross-section of the sample consisting of the suspended CGT/WSe₂ heterostructure membrane and the reference WSe₂ membrane of the same flake. Bottom panel: Optical image of the sample with specific membranes indicated. Scale bar: 16 μm. **b** Measured resonance frequencies f_0 of the membranes in (a). Solid green line - the fitted model of the resonance frequency of the CGT/WSe₂ heterostructure (equation (4)). Light green region - the allowed higher and lower boundary of the model due to the uncertainties in $h_{1,2}$, $E_{1,2}$ and $f_0^2(T_0)$. Insets: Schematic of the collinear and random magnetic spin arrangement in a bilayer of CGT in the ferromagnetic (FM) and the paramagnetic (PM) phases respectively. **c** Mechanical damping Q^{-1} as a function temperature. **d** Filled blue circles - $\frac{d(f_0^2)}{dT}$ of the CGT/WSe₂ heterostructure as a function of temperature. Connected magenta circles - the thermal expansion coefficient of bulk CGT [5]. The black vertical dashed lines in (b-d) indicate the measured $T_C^* = 58 \pm 0.5$ K as determined from the peak position of $\frac{d(f_0^2)}{dT}$.

the negative $\alpha_{\text{CGT}}(T)$ near T_C of CGT, such that the total membrane stress remains tensile and f_0 can be used to probe $\alpha(T)$ even below T_C .

We measure $f_0(T)$ of the suspended CGT/WSe₂ heterostructure together with a reference drum of the same WSe₂ flake (Fig. 3b). The $f_{0,\text{WSe}_2}(T)$ follows a monotonous increase trend with decreasing temperature (filled orange circles), as expected from its positive $\alpha_{\text{WSe}_2}(T)$ [27, 44]. In contrast, $f_{0,\text{CGT/WSe}_2}(T)$ has a downturn with decreasing temperature near the transition temperature (filled blue circles). This behaviour is distinct from the bare CGT resonator (Fig. 2c) and is due to the positive thermal expansion coefficient of the WSe₂ layer, which maintains a tensile total strain of the heterostructure. We also plot the mechanical dissipation, the inverse of a quality factor $Q^{-1}(T)$, of both the WSe₂ and CGT/WSe₂ resonators in Fig. 3c. A notable peak in $Q_{\text{CGT/WSe}_2}(T)$ is visible at $T = 58$ K. We attribute this observation to an increase of the thermoelastic damping [45, 46] expected near T_C in magnetic resonators [26].

This observation is supported by the measured maximum in $\frac{d(f_0^2)}{dT}$ (filled blue circles) [26] at 58 ± 0.5 K, the temperature which we define as T_C^* and indicate by the black vertical dashed lines in Fig. 3d. The observed maximum at T_C^* relates to the peak in the thermal expansion coefficient of CGT at T_C (filled magenta circles) that is shifted to lower temperatures in comparison to its bulk values of 60 – 66 K [2, 5].

We model the resonance frequency of a heterostructure $f_{0,h}(T)$ by modifying equation (2) to describe the observations in Fig. 3b. We describe the total thermally accumulated tension of the CGT/WSe₂ heterostructure as a sum of individual tensions in each layer [28, 32]:

$$n_{\text{th}}(T) = n_{\text{th},1}(T) + n_{\text{th},2}(T) \quad (3)$$

$$= \frac{E_1 h_1}{(1 - \nu_1)} \epsilon_{\text{th},1}(T) + \frac{E_2 h_2}{(1 - \nu_2)} \epsilon_{\text{th},2}(T).$$

We assume that the slippage between the layers is negligible. Therefore, we obtain the final equation for the

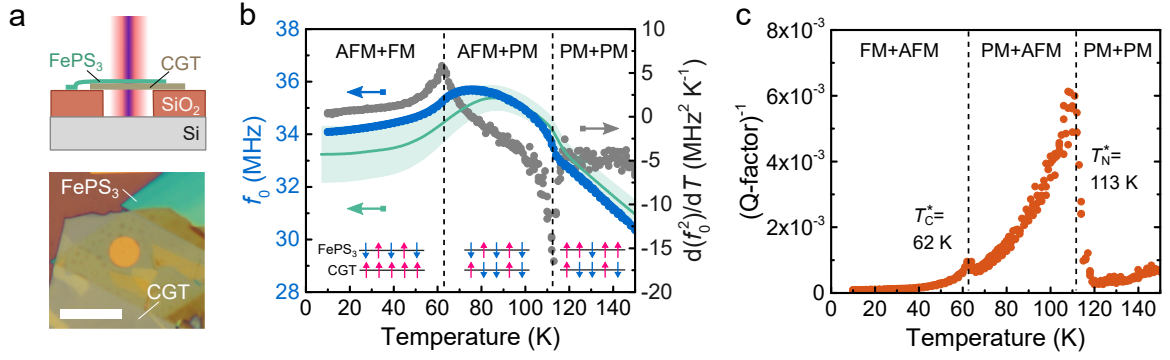


FIG. 4. Mechanical properties of a CGT/FePS₃ (19.8 ± 0.2 nm/ 18.0 ± 0.1 nm) heterostructure membrane with a radius $r = 2.5$ μm. **a** Top panel: A schematic cross-section of the suspended heterostructure membrane. Bottom panel: The optical image of the sample with the CGT/FePS₃ heterostructure. Scale bar: 10 μm. **b** Filled blue circles - the measured resonance frequency as a function of temperature. Filled grey circles — the temperature derivative of f_0^2 . Solid green line - the heterostructure resonance frequency model as described by equation (4). The light green region indicates the higher and lower boundary of the model allowed due to the uncertainties in $h_{1,2}$, E_{CGT} and $f_0^2(T_0)$. The insets: Schematic pictures of a magnetic spin configuration in FePS₃ and CGT layers in corresponding combinations of antiferromagnetic (AFM), ferromagnetic (FM) and paramagnetic (PM) phases. **c** The mechanical damping Q^{-1} as a function of temperature, in which the filled orange circles represent the measured data of the CGT/FePS₃ heterostructure. The black vertical dashed lines in (b) and (c) represent the measured $T_C^* = 62 \pm 1$ K of CGT and $T_N^* = 113 \pm 1$ K of FePS₃ as determined from positions of extrema in $\frac{d(f_0^2)}{dT}$ in (b).

resonance frequency of the heterostructure as:

$$f_{0,h}(T) = \sqrt{\left(\frac{2.4048}{2\pi r}\right)^2 \frac{1}{\rho_1 h_1 + \rho_2 h_2} n_{th}(T) + f_0^2(T_0)}, \quad (4)$$

where n_{th} is given by equation (3). We plot the model of equation (4) for the CGT/WSe₂ heterostructure in Fig. 3b (solid green line). In doing so, we use the bulk $\alpha_{\text{CGT}}(T)$ values [5], $\rho_{\text{CGT}} = 6091$ kg m⁻³ [5], $\nu_{\text{CGT}} = 0.22$ [35], and $E_{\text{CGT}} = 56.2 \pm 8.2$ GPa for CGT; $\epsilon_{th,WSe_2}(T)$ extracted from the measured $f_{0,WSe_2}(T)$ of the reference drum using equation (2), $\rho_{WSe_2} = 9320$ kg m⁻³ [43, 47], $\nu_{WSe_2} = 0.19$ [43, 48] and $E_{WSe_2} = 167.1 \pm 0.7$ GPa (measured for this membrane using the nanoindentation method described above, which is consistent with previous studies [43]) for WSe₂; and $f_0(94 \text{ K}) = 27.2 \pm 0.4$ MHz. The resulting model reproduces the experiment qualitatively, yet lacks quantitative agreement above T_C , most likely due to the overestimation of $\alpha_{\text{CGT}}(T)$ for thin layers of CGT in contrast to its bulk value [5].

Magnetic heterostructures.

The presented methodology is not limited exclusively to the use of WSe₂, given that the thermal expansion coefficient of the added material is large and positive. To explore the possibility of detecting two magnetic phase transitions in the same membrane and also the possibility of having emergent properties arising from a coupling between the two flakes, we fabricate a heterostructure membrane made of a ferromagnetic CGT covered

by an antiferromagnetic FePS₃ layer, which exhibits positive $\alpha_{\text{FePS}_3}(T)$ [26], as shown in Fig. 4a. Using the methods described above, we measure the resonance frequency of this suspended structure as a function of temperature. In Fig. 4b, we plot experimental $f_0(T)$ (filled blue circles) together with its $\frac{d(f_0^2(T))}{dT}$ (filled grey circles). The temperature derivative of f_0^2 shows two clear extrema, indicated by black vertical dashed lines: the first one at $T_C^* = 62 \pm 1$ K we attribute to the T_C of CGT [2, 5]; the second one at $T_N^* = 113 \pm 1$ K corresponds to the Néel temperature, T_N , of FePS₃ [3, 26]. We plot the model of equation (4) in Fig. 4b (solid green line) for the CGT/FePS₃ heterostructure using material parameters of CGT from literature [5, 26, 35] and E_{CGT} as determined from Fig. 1; $E_{\text{FePS}_3} = 103$ GPa, $\rho_{\text{FePS}_3} = 3375$ kg m⁻³, $\nu_{\text{FePS}_3} = 0.304$ [26, 49] for FePS₃; and $f_0(150 \text{ K}) = 30.9 \pm 0.7$ MHz. The model describes the experiment well with some deviations at low temperatures similar to the ones described above in Fig. 3c. In addition, we observe two peaks in $Q^{-1}(T)$, displayed in Fig. 4c, that we attribute to increased thermoelastic damping near the phase transition [26, 45, 46]. The temperatures of these peaks coincide with the extrema from Fig. 4b, confirming the phase transitions in CGT and FePS₃.

Electrostatic strain tuning of T_C .

Since strong magnetostriction is responsible for the large anomalies in the mechanical response of CGT membranes at T_C [5, 14] (Fig. 1), we expect that the inverse effect should also be present allowing us to tune the T_C

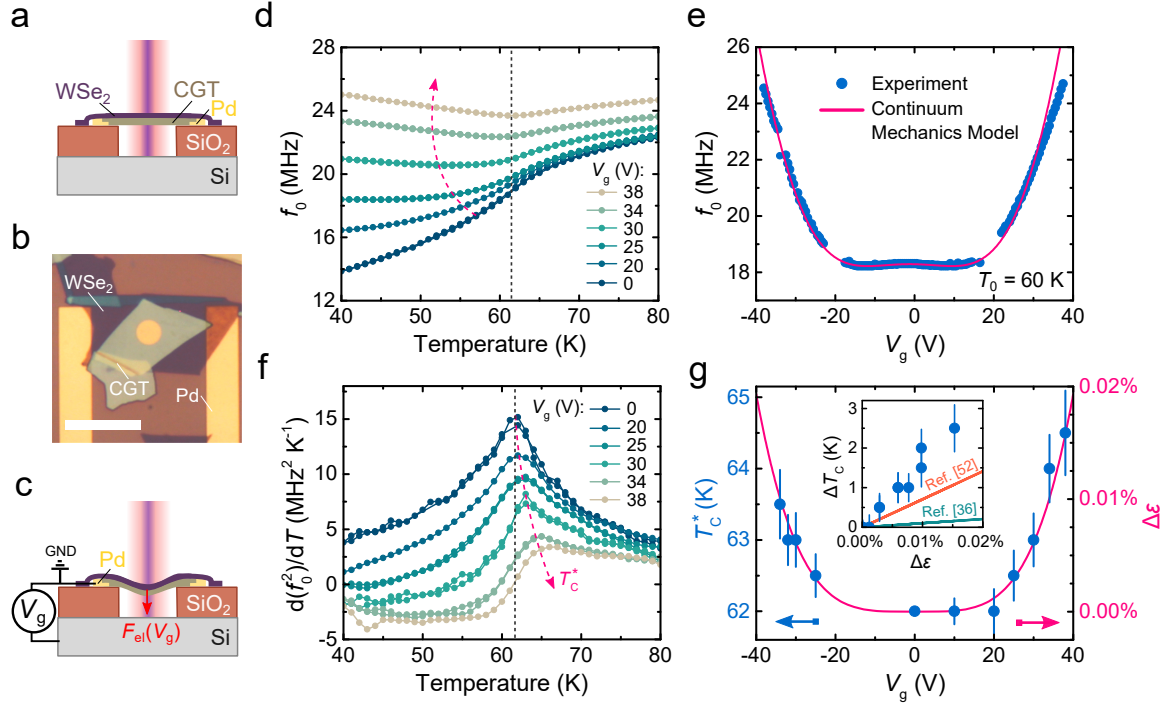


FIG. 5. Curie temperature enhancement as a function of strain in a suspended CGT/WSe₂ heterostructure (19.7 ± 0.1 nm/ 8.5 ± 0.2 nm). **a** The schematic cross-section of the suspended CGT/WSe₂ heterostructure membrane. **b** The optical image of the heterostructure with materials indicated. Membrane radius: $r = 4 \mu\text{m}$. Scale bar: $12 \mu\text{m}$. **c** The schematics of the electrostatic strain-tuning principle. **d** Measured resonance frequencies f_0 of the heterostructure membrane as a function of temperature for different gate voltages V_g . **e** Filled blue circles - the measured resonance frequency as a function of V_g at 60 K. Solid magenta line - the continuum model mechanics model fit [50, 51]. **f** The temperature derivative of f_0^2 as a function of temperature for different V_g . The black vertical dashed lines in (d) and (e) show the peak position in $\frac{d(f_0^2)}{dT}$ at $V_g = 0$ V. **g** Filled blue circles — the shift in measured T_C^* as a function of V_g extracted from the peak position in (e). Solid magenta line - the estimate of electrostatically induced strain $\Delta\epsilon$ as a function of V_g . The inset shows $\Delta T_C = T_C^*(V_g) - T_C^*(0\text{ V})$ as a function of added voltage induced strain $\Delta\epsilon$ in addition to calculations from Li and Yang [36] (solid green line) and from Dong et al [52] (solid orange line). The vertical error bars in T_C^* were estimated from determining the peak position in (e) within 2% accuracy in the measured maximum.

via strain [26, 29]. To study this effect, we fabricate another CGT/WSe₂ heterostructure membrane contacted to Pd electrodes, as shown in Fig. 5a-c. We apply a gate voltage V_g between the heterostructure membrane and the bottom Si substrate electrode to induce an electrostatic force, F_{el} , that pulls the membrane down and thus strains the CGT/WSe₂ stack. In Fig. 5d, we show the measured f_0 of the heterostructure membrane as a function of temperature for six different values of V_g . A notable increase of f_0 as a function of V_g is evident which is attributed to the electrostatic strain introduced. To describe the gate dependence of the resonance frequency, we show the $f_0(V_g)$ relationship near the phase transition temperature at $T_0 = 60$ K in Fig. 5e. We fit the measurement data to a continuum mechanics model of a circular membrane resonator [50, 51] (see Experimental Section), which describes the experiment well. We thus estimate the added electrostatic strain [29, 51] as $\Delta\epsilon \approx \frac{2}{3} \left(\frac{\epsilon_0 r}{8g_0^2 n(T_0)} \right)^2 V_g^4$, where ϵ_0 is the dielectric permit-

tivity of vacuum, and $n(T_0) = 2.538 \pm 0.003 \text{ nm}^{-1}$ the total tension in the suspended heterostructure at $T_0 = 60$ K (extracted from the fit in Fig. 5e).

Apart from the effect of electrostatically induced strain on $f_0(V_g)$ in Fig. 5d, the characteristic feature in the $f_0(T)$ curve, that we attribute to the Curie temperature of CGT [26], shifts to higher temperatures. This trend becomes even more apparent in Fig. 5f, where we plot $\frac{d(f_0^2)}{dT}$ for six different V_g . We extract T_C^* from the peak positions in $\frac{d(f_0^2)}{dT}$ for multiple V_g and plot it against the gate-induced strain, $\Delta\epsilon$, in Fig. 5g. The observed enhancement in T_C^* qualitatively agrees with the added tensile strain dependence symmetrically both for positive and negative V_g as shown in Fig. 5g. This indicates that the gate-induced strain has a dominant contribution to the change in the $T_C^*(V_g)$ instead of a field effect [6, 7]. In the inset of Fig. 5g, we plot the experimental $\Delta T_C = T_C^*(V_g) - T_C^*(0\text{ V})$ versus the estimated strain $\Delta\epsilon$, together with predictions from density-functional theory

calculations for 2D CGT by Li and Yang [36], considering the direct exchange interaction (solid green line), and by Dong et al [52], attributing the enhancement of T_C to the super-exchange interaction via Cr-Te-Cr bonds (solid orange line). The closer experimental agreement with the results of Dong et al. [52] suggests that it is the decreasing energy difference between $3d$ orbitals of Cr and $5p$ orbitals of Te in nearly $\sim 90^\circ$ Cr-Te-Cr bonds of CGT that is likely to contribute to the enhancement of T_C^* as a function of strain [52]. Interestingly, we observed that the maximal T_C^* increase by mechanical strain was as much as 2.5 ± 0.6 K at $\Delta\epsilon \approx 0.016\%$. This is comparable to what was previously achieved in bulk CGT by applying an out-of-plane magnetic field of $0.7 - 1$ T [2, 8], proving that strain-based nanomechanical methods provide a compelling route for controlling and probing magneto-elastic coupling in ferromagnetic 2D layers and heterostructures.

DISCUSSION

In conclusion, we have probed the mechanical properties of CGT membranes by both static and dynamic nanomechanical means. We demonstrated that due to CGT's strong magnetostriction [5, 14] and large negative thermal expansion near T_C , bare CGT membranes experience strong resonance frequency reductions near their ferromagnetic Curie temperature and an accumulation of compressive strain. The compressive strain can produce buckling, wrinkling or sagging of the CGT layers, that significantly complicates the analysis for nanomechanical measurements of T_C [26]. We showed that this issue can be solved by integrating CGT in heterostructures with other materials with positive thermal expansion coefficients. This methodology can also be applied using materials that have phase transitions themselves, which we demonstrate by probing both T_N of FePS₃ and T_C of CGT within a single measurement of a CGT/FePS₃ heterostructure. The presented measurements and methodologies for nanomechanical characterisation of magnetic heterostructures open up possibilities to investigate magnetic properties that are the result of interfacial interactions in 2D magnetic heterostructures membranes [53, 54], allowing also novel magnetic properties to be discovered near the monolayer limit while excluding substrate interactions. In addition, we expect that focused studies of the mechanical dissipation in such heterostructures as a function of temperature and strain could in the future provide more insights to thermodynamics and heat transport in 2D materials involved [26, 55, 56]. Finally, we showed that T_C of CGT can be enhanced by gate-induced electrostatic straining, demonstrating control of magnetic order in these ferromagnetic heterostructures using strain. We anticipate that these studies in the future will lead to the development of membrane devices with gate-controlled magnetic actuation [57] for low-power spintronic applications.

METHODS

Device fabrication and characterization. We first pattern a diced Si/SiO₂ wafer and define circular holes with a radius of $r = 1 - 2.5$ μm and cavity depth of $g_0 = 285$ nm using an e-beam lithography and reactive ion etching. SiO₂ provides an electrical insulation between subsequently transferred 2D material membranes and the bottom Si electrode. To realize electrical contact to some samples for electrostatic experiments, Pd electrodes are pre-patterned on top of Si/SiO₂ chips by a lift-off technique. To create suspended membranes, thin flakes of CGT, FePS₃ and WSe₂ crystals are mechanically exfoliated and transferred on a pre-patterned chip by the all-dry viscoelastic stamping method [58] directly after exfoliation. Flakes of van der Waals crystals are exfoliated from high quality synthetically grown crystals with known stoichiometry. Using the same method, flakes are deterministically stacked on top of each other forming heterostructures. We stack FePS₃ and WSe₂ flakes on top of CGT to minimise the exposure time of the suspended CGT layers to air. Subsequently, samples were kept in an oxygen-free environment to avoid degradation.

Atomic force microscopy characterisation. Atomic force microscopy height profile scans and inspection are performed in tapping mode on a Bruker Dimension FastScan AFM. We use cantilevers with spring constants of $k_c = 30 - 40$ Nm^{-1} for inspection. Error bars on reported thickness values are determined by measuring multiple profile scans of the same flake. For force nanoindentation experiments, we use two different cantilevers with spring constants of $k_c = 8.87 \pm 0.08$ Nm^{-1} and $k_c = 18.90 \pm 0.11$ Nm^{-1} . k_c for each cantilever was calibrated using thermal and solid surface deflection. We use cantilever tips with a tip radius of $\sim 7 - 10$ nm, as confirmed by scanning electron microscope imaging.

Laser interferometry measurements. The sample is mounted on a xy piezopositioning stage inside a dry optical 4 K cryostat Montana Instruments Cryostation s50. A local sample heater is used to perform temperature sweeps at a rate of ~ 3 K per minute, keeping the pressure in the chamber below 10^{-6} mbar. A power modulated blue diode laser of $\lambda = 405$ nm is used to optothermally excite the motion of the membrane. Membrane displacement is then measured using a laser interferometer with a He-Ne laser beam of $\lambda = 632$ nm focused on the suspended membrane. In doing so, the interfering reflections from the membrane and the Si electrode underneath are recorded using a photodiode and processed by a vector network analyzer. All measurements were performed at incident laser powers of $P_{\text{red}} \leq 8$ μW and $P_{\text{blue}} \leq 1$ μW . Laser spot size is on the order of ~ 1 μm . During the data acquisition it is checked for all membranes that resonance frequency changes due to laser heating are insignificant. During data acquisition temperature is kept constant with ~ 10 mK stability by the local heater and a closed feedback loop controller.

Continuum mechanics model of electrostatically strained circular membrane A membrane suspended over a circular cavity forms a capacitor with a bottom gate electrode underneath. The change in gate voltage causes the membrane to deflect, tuning the tension and producing a shift in the resonance frequency. The resonance frequency of the fundamental vibration mode of the drum as a function of gate voltage is described as [50]:

$$f_0(V_g) = \frac{1}{2\pi} \sqrt{\frac{1}{m_{\text{eff}}} \left[\frac{2\pi E h \epsilon_0}{1 - \nu^2} + \frac{8\pi E h}{(1 - \nu^2) r^2} z_g^2 - \frac{1}{2} \frac{\partial^2 C_g}{\partial z^2} V_g^2 \right]}, \quad (5)$$

where $z_g \approx \frac{\epsilon_0 r^2}{8g_0^2 n(T_0)} V_g^2$ is the maximal deflection at the membrane centre [51], $\frac{\partial^2 C_g}{\partial z^2} \approx \frac{0.542\epsilon_0 \pi r^2}{g_0^3}$ the second derivative of capacitance [51, 59], and $m_{\text{eff}} = 0.27\rho h \pi r^2$ the effective mass. In the case of a heterostructure membrane, material parameters are substituted for the heterostructure analogues [28]: $E = \frac{E_1 h_1 + E_2 h_2}{h_1 + h_2}$, $\rho = \frac{\rho_1 h_1 + \rho_2 h_2}{h_1 + h_2}$, $\nu = \frac{\nu_1 h_1 + \nu_2 h_2}{h_1 + h_2}$, and $h = h_1 + h_2$. For the CGT/WSe₂ heterostructure (19.7 ± 0.1 nm/ 8.5 ± 0.2 nm) in Fig. 5 we use the following material parameters: $E = 89.6$ GPa, $h = 28.2$ nm, $\nu = 0.21$, $\rho = 7064$ kg m⁻³. We extract $\epsilon = 0.079 \pm 0.004\%$, $\frac{\partial^2 C_g}{\partial z^2} = 3.46 \pm 0.11$ mFm⁻² and $m_{\text{eff}} = 996.45$ fg from the fit in Fig. 5e, that are close to the expected values [51, 59] of $\frac{\partial^2 C_g}{\partial z^2} = 2.61$ mFm⁻² and $m_{\text{eff}} = 675.9$ fg.

Acknowledgements

The authors thank B. Simon for continuous support and feedback on the manuscript. M.Š., M.L., H.S.J.v.d.Z. and P.G.S. acknowledge funding from the European Union's Horizon 2020 research and innovation program under grant agreement number 881603. H.S.J.v.d.Z., E.C. and S.M.-V. thank COST Action MOLSPIN CA15128; E.C. and S.M.-V. acknowledge the financial support from the European Union (ERC AdG Mol-2D 788222), the Spanish MICINN (MAT2017-89993-R co-financed by FEDER and Excellence Unit "María de Maeztu", CEX2019-000919-M) and the Generalitat Valenciana (Prometeo program and PO FEDER Program, ref. IDIFEDER/2018/061 and IDIFEDER/2020/063). W.X., S.J., and W.H. thank National Natural Science Foundation of China (11974025).

Author Contributions

M.Š., S.K., E.C., H.S.J.v.d.Z., T.v.d.S. and P.G.S. conceived the experiments. M.Š. performed the laser interferometry measurements. M.Š. and M.L. fabricated and inspected the samples. S.M.-V. and E.C. synthesized and characterized the FePS₃ crystals. W.X., S.J. and W.H. synthesized and characterized the Cr₂Ge₂Te₆ crystals. M.Š., S.K. and B.J.M.S. analyzed and modeled the experimental data. H.S.J.v.d.Z., T.v.d.S. and P.G.S. supervised the project. The paper was jointly written by all authors with a main contribution from M.Š. All authors discussed the results and commented on the paper.

REFERENCES

- [1] Huang, B. *et al.* Layer-dependent ferromagnetism in a van der Waals crystal down to the monolayer limit. *Nature* **546**, 270 (2017).
- [2] Gong, C. *et al.* Discovery of intrinsic ferromagnetism in two-dimensional van der Waals crystals. *Nature* **546**, 265 (2017).
- [3] Lee, J.-U. *et al.* Ising-type magnetic ordering in atomically thin FePS₃. *Nano Lett.* **16**, 7433 (2016).
- [4] Gibertini, M., Koperski, M., Morpurgo, A. F. & Novoselov, K. S. Magnetic 2D materials and heterostructures. *Nat. Nanotechnol.* **14**, 408 (2019).
- [5] Carteaux, V., Brunet, D., Ouvrard, G. & Andre, G. Crystallographic, magnetic and electronic structures of a new layered ferromagnetic compound Cr₂Ge₂Te₆. *J. Phys. Condens. Matter.* **7**, 69 (1995).
- [6] Verzhbitskiy, I. A. *et al.* Controlling the magnetic anisotropy in Cr₂Ge₂Te₆ by electrostatic gating. *Nat. Electron.* **3**, 460 (2020).
- [7] Wang, Z. *et al.* Electric-field control of magnetism in a few-layered van der Waals ferromagnetic semiconductor. *Nat. Nanotechnol.* **13**, 554 (2018).
- [8] Selter, S., Bastien, G., Wolter, A. U. B., Aswartham, S. & Büchner, B. Magnetic anisotropy and low-field magnetic phase diagram of the quasi-two-dimensional ferromagnet Cr₂Ge₂Te₆. *Phys. Rev. B* **101**, 014440 (2020).
- [9] Sun, Y. *et al.* Effects of hydrostatic pressure on spin-lattice coupling in two-dimensional ferromagnetic Cr₂Ge₂Te₆. *Appl. Phys. Lett.* **112**, 072409 (2018).
- [10] Sakurai, T. *et al.* Pressure control of the magnetic anisotropy of the quasi-two-dimensional van der Waals ferromagnet Cr₂Ge₂Te₆. *Phys. Rev. B* **103**, 024404 (2021).
- [11] Wang, N. *et al.* Transition from ferromagnetic semiconductor to ferromagnetic metal with enhanced curie temperature in Cr₂Ge₂Te₆ via organic ion intercalation. *J. Am. Chem. Soc.* **141**, 17166 (2019).
- [12] Gupta, V. *et al.* Manipulation of the van der Waals magnet Cr₂Ge₂Te₆ by spin-orbit torques. *Nano Lett.* **20**, 7482 (2020).
- [13] Ostwal, V., Shen, T. & Appenzeller, J. Efficient spin-orbit torque switching of the semiconducting van der Waals ferromagnet Cr₂Ge₂Te₆. *Adv. Mater.* **32**, 1906021 (2020).
- [14] Tian, Y., Gray, M. J., Ji, H., Cava, R. J. & Burch, K. S. Magneto-elastic coupling in a potential ferromagnetic 2D atomic crystal. *2D Mater.* **3**, 025035 (2016).
- [15] Kozlenko, D. P. *et al.* Spin-induced negative thermal expansion and spin-phonon coupling in van der Waals

- material CrBr₃. *npj Quantum Mater.* **6**, 19 (2021).
- [16] Casto, L. D. *et al.* Strong spin-lattice coupling in CrSiTe₃. *APL Mater.* **3**, 041515 (2015).
- [17] McGuire, M. A., Dixit, H., Cooper, V. R. & Sales, B. C. Coupling of crystal structure and magnetism in the layered, ferromagnetic insulator CrI₃. *Chem. Mater.* **27**, 612–620 (2015).
- [18] Schneeloch, J. A. *et al.* Gapless Dirac magnons in CrCl₃ (2021). Preprint at <https://arxiv.org/abs/2110.10771v1>.
- [19] Miao, F., Liang, S.-J. & Cheng, B. Straintronics with van der Waals materials. *npj Quantum Mater.* **6**, 59 (2021).
- [20] Yang, S., Chen, Y. & Jiang, C. Strain engineering of two-dimensional materials: Methods, properties, and applications. *InfoMat* **3**, 397–420 (2021).
- [21] Chen, C. *et al.* Performance of monolayer graphene nanomechanical resonators with electrical readout. *Nat. Nanotechnol.* **4**, 861 (2009).
- [22] Zhang, X. *et al.* Dynamically-enhanced strain in atomically thin resonators. *Nat. Commun.* **11**, 5526 (2020).
- [23] Chen, C. *et al.* Graphene mechanical oscillators with tunable frequency. *Nat. Nanotechnol.* **8**, 923 (2013).
- [24] Lemme, M. C. *et al.* Nanoelectromechanical sensors based on suspended 2D materials. *Research* **2020**, 8748602 (2020).
- [25] Lee, C., Wei, X., Kysar, J. W. & Hone, J. Measurement of the elastic properties and intrinsic strength of monolayer graphene. *Science* **321**, 5887 (2008).
- [26] Šiškins, M. *et al.* Magnetic and electronic phase transitions probed by nanomechanical resonators. *Nat. Commun.* **11**, 2698 (2020).
- [27] Morell, N. *et al.* High quality factor mechanical resonators based on WSe₂ monolayers. *Nano Lett.* **16**, 5102 (2016).
- [28] Ye, F., Lee, J. & Feng, P. X.-L. Atomic layer MoS₂-graphene van der Waals heterostructure nanomechanical resonators. *Nanoscale* **9**, 18208 (2017).
- [29] Jiang, S., Xie, H., Shan, J. & Mak, K. F. Exchange magnetostriction in two-dimensional antiferromagnets. *Nat. Mater.* **19**, 1295 (2020).
- [30] Ni, Z. *et al.* Imaging the Néel vector switching in the monolayer antiferromagnet MnPSe₃ with strain-controlled Ising order. *Nat. Nanotechnol.* **16**, 782–787 (2021).
- [31] Liu, K. *et al.* Elastic properties of chemical-vapor-deposited monolayer MoS₂, WS₂, and their bilayer heterostructures. *Nano Lett.* **14**, 5097 (2014).
- [32] Kim, S., Yu, J. & van der Zande, A. M. Nanoelectromechanical drumhead resonators from two-dimensional material bimorphs. *Nano Lett.* **18**, 6686 (2018).
- [33] Novoselov, K. S., Mishchenko, A., Carvalho, A. & Neto, A. H. C. 2D materials and van der Waals heterostructures. *Science* **353**, aac9439 (2016).
- [34] Castellanos-Gomez, A. *et al.* Elastic properties of freely suspended MoS₂ nanosheets. *Adv. Mater.* **24**, 772 (2012).
- [35] de Jong, M. *et al.* Charting the complete elastic properties of inorganic crystalline compounds. *Sci. Data* **2**, 150009 (2015).
- [36] Li, X. & Yang, J. CrXTe₃ (X = Si, Ge) nanosheets: two dimensional intrinsic ferromagnetic semiconductors. *J. Mater. Chem. C* **2**, 7071 (2014).
- [37] Cantos-Prieto, F. *et al.* Layer-dependent mechanical properties and enhanced plasticity in the van der Waals chromium trihalide magnets. *Nano Lett.* **21**, 3379–3385 (2021).
- [38] Castellanos-Gomez, A. *et al.* Single-layer MoS₂ mechanical resonators. *Adv. Mater.* **25**, 6719 (2013).
- [39] Lyon, K. G., Salinger, G. L., Swenson, C. A. & White, G. K. Linear thermal expansion measurements on silicon from 6 to 340 K. *J. Appl. Phys.* **48**, 865 (1977).
- [40] Chen, T., Pauly, M. & Reis, P. M. A reprogrammable mechanical metamaterial with stable memory. *Nature* **589**, 386 (2021).
- [41] Mahboob, I. & Yamaguchi, H. Bit storage and bit flip operations in an electromechanical oscillator. *Nat. Nanotechnol.* **3**, 275 (2008).
- [42] Roodenburg, D., Spronck, J. W., van der Zant, H. S. J. & Venstra, W. J. Buckling beam micromechanical memory with on-chip readout. *Appl. Phys. Lett.* **94**, 183501 (2009).
- [43] Zhang, R., Koutsos, V. & Cheung, R. Elastic properties of suspended multilayer WSe₂. *Appl. Phys. Lett.* **108**, 042104 (2016).
- [44] Çakır, D., Peeters, F. M. & Sevik, C. Mechanical and thermal properties of h-MX₂ (M = Cr, Mo, W; X = O, S, Se, Te) monolayers: A comparative study. *Appl. Phys. Lett.* **104**, 203110 (2014).
- [45] Lifshitz, R. & Roukes, M. L. Thermoelastic damping in micro- and nanomechanical systems. *Phys. Rev. B* **61**, 5600 (2000).
- [46] Sun, Y., Fang, D. & Soh, A. K. Thermoelastic damping in micro-beam resonators. *Int. J. Solids. Struct.* **43**, 3213 (2006).
- [47] Agarwal, M. & Wani, P. Growth conditions and crystal structure parameters of layer compounds in the series Mo_{1-x}W_xSe₂. *Mater. Res. Bull.* **14**, 825 (1979).
- [48] Zeng, F., Zhang, W.-B. & Tang, B.-Y. Electronic structures and elastic properties of monolayer and bilayer transition metal dichalcogenides MX₂ (M = Mo, W; X = O, S, Se, Te): a comparative first-principles study. *Chinese Phys. B* **24**, 097103 (2015).
- [49] Hashemi, A., Komsa, H.-P., Puska, M. & Krasheninnikov, A. V. Vibrational properties of metal phosphorus trichalcogenides from first-principles calculations. *J. Phys. Chem. C* **121**, 27207 (2017).
- [50] Chen, C. *PhD thesis* (Columbia University, 2013).
- [51] Weber, P., Güttinger, J., Tsioutsios, I., Chang, D. E. & Bachtold, A. Coupling graphene mechanical resonators to superconducting microwave cavities. *Nano Lett.* **14**, 2854 (2014).
- [52] Dong, X.-J., You, J.-Y., Zhang, Z., Gu, B. & Su, G. Great enhancement of curie temperature and magnetic anisotropy in two-dimensional van der Waals magnetic semiconductor heterostructures. *Phys. Rev. B* **102**, 144443 (2020).
- [53] Zhang, L. *et al.* Proximity-coupling-induced significant enhancement of coercive field and Curie temperature in 2D van der Waals heterostructures. *Adv. Mater.* **32**, 2002032 (2020).
- [54] Wang, Y. *et al.* Modulation doping via a two-dimensional atomic crystalline acceptor. *Nano Lett.* **20**, 8446–8452 (2020).
- [55] Dolleman, R. J. *et al.* Optomechanics for thermal characterization of suspended graphene. *Phys. Rev. B* **96**, 165421 (2017).
- [56] Morell, N. *et al.* Optomechanical measurement of thermal transport in two-dimensional MoSe₂ lattices. *Nano Lett.* **19**, 3143 (2019).

- [57] Ben-Shimon, Y. & Ya'akovovitz, A. Magnetic excitation and dissipation of multilayer two-dimensional resonators. *Appl. Phys. Lett.* **118**, 063103 (2021).
- [58] Castellanos-Gomez, A. *et al.* Deterministic transfer of two-dimensional materials by all-dry viscoelastic stamping. *2D Mater.* **1**, 011002 (2014).
- [59] Will, M. *et al.* High quality factor graphene-based two-dimensional heterostructure mechanical resonator. *Nano Lett.* **17**, 5950 (2017).